Tunable Multimodal Guided Surface Lattice Resonances in Index-Discontinuous Environments

Suichu Huang[1], Kan Yao[2], Wentao Huang[1], Xuezheng Zhao[1, *], Yuebing Zheng[2, *], Yunlu Pan[1, *]

1 Key Laboratory of Micro-Systems and Micro-Structures Manufacturing of Ministry of Education and School of Mechatronics Engineering, Harbin Institute of Technology, Harbin 150001, China

2 Walker Department of Mechanical Engineering, Material Science and Engineering Program and Texas Materials Institute, The University of Texas at Austin, Austin, TX 78712, United States

* Corresponding author. Email: zhaoxz@hit.edu.cn, zheng@austin.utexas.edu, yunlupan@hit.edu.cn

Abstract

Surface lattice resonances (SLRs) in metasurfaces are promising in applications of sub-wavelength devices, owning properties such as high quality (high-Q) factors, large local field enhancement and extensive long-range interaction. The tunable peak position and multimodal resonances of SLRs further enhance their appeal for flexible and multi-wavelength light-matter interactions. Despite these advantages, the realization of tunable multimodal SLRs often requires reconfiguring the lattices, leading to limited tunability. Furthermore, current high-Q SLR implementations necessitate a homogeneous dielectric environment, restricting potential applications such as biosensors that are typically operated in an aqueous or air cladding on a substrate. Here we present guided-SLRs (gSLRs), which are easily accessible in index-discontinuous environments while retaining the multimodal property and straightforward tunability of mode number, resonance wavelengths and mode coupling strengths. The gSLRs are achieved by coupling the scattered light from metasurface units into a slab waveguide, creating a light propagating channel in the lattice plane within an index-asymmetric environment. Tailoring the radiation pattern of individual units with guided transverse electric (TE) and transverse magnetic (TM) modes, multimodal resonances in both orthogonal and parallel coupling directions are accomplished. The mode number and resonance wavelengths can be easily controlled by adjusting the waveguide configuration, while the mode coupling strength is tuned by the vertical position of lattices in the slab. Further shift of the multimodal gSLRs from visible to near-infrared is achieved by

introducing a gold backplane. The easy-to-access, flexibly tunable and multimodal gSLRs in inhomogeneous media offer a promising solution to advancing the realization of ultrathin and ultracompact nano-optical and optoelectronic devices.

Key Words: Surface lattice resonances, metasurfaces, multimodal resonances, tunability, radiation pattern, waveguide

1 Introduction

With the ability to confine light in the sub-wavelength range and to largely enhance local fields, plasmonic nanostructures have garnered significant interest in many domains of optics and photonics research, such as nanolasing[1,2], optical switching[3,4], biosensing[5,6], non-linear optical processes[7,8], metasurfaces[9,10] and bound states in the continuum[11,12]. Individual sub-wavelength plasmonic nanostructures support localized surface plasmon resonances (LSPRs), where the free-electron plasma at the metal-dielectric interface couples to the oscillating electromagnetic waves[13]. The local field enhancement allows plasmonic nanoparticles to play rich roles in studying and utilizing light-matter interactions[14,15], such as sensing[16,17]. However, potential applications of plasmonic nanoparticles or clusters are hindered by their low quality-factors (Q-factors), primarily due to the intrinsic Ohmic losses of plasmonic materials at optical frequencies[18-20].

A practical way to significantly increase the Q-factors of plasmonic nanostructures is arranging nanoparticles into organized lattices. When the radiative LSPR modes of individual nanoparticles match the in-plane diffraction modes of a lattice, a so-called surface lattice resonance (SLR) emerges, where the loss of individual units is supplemented by the scattered field from adjacent ones, resulting in high-Q resonances[18,21-23]. Through careful design, plasmonic metasurfaces with a Q-factor exceeding 2000 have been reported[20].

A vital prerequisite for the excitation of high-Q in-plane SLRs is index-matching of the superstrate and substrate[21,24,25]. An index discontinuity at the interface tends to destruct the in-plane coupling within an array[25] but is necessary for many fabrication techniques and in application scenarios. Immersing the substrate-supported array into an index-matching liquid can be expedient[26,27] but is not a versatile solution for different types of applications, for example, biosensing, where the superstrate is usually air or water[28,29]. Recently, a few SLRs in

index-mismatched environments have been demonstrated[30-34], which are implemented by engineering the particle geometry[30,31] or introducing a metal substrate[32-34]. However, the obtained Q-factors of SLRs on a dielectric substrate are low and explanations of SLRs on a metal substrate are ambiguous. A theoretically unequivocal and widely adaptable method to realize high-Q resonances in asymmetrical environments is still in demand.

Although most SLR studies focus on single-mode resonance, some applications, for example, multimodal lasing[35,36], require enhanced light-matter interactions at different wavelengths simultaneously, leading to the exploration of multimodal SLRs[37-41]. Implementations based on lattice hybridization[37,38], band structure engineering[36,39] and multi-reflection at a close boundary[40,41] have been demonstrated. However, these methods involve elaborate lattice design, have a limited number of SLR modes and lack tunability. In the meantime, the control of mode coupling strength has merely been reported. A simple way to realize abundant resonant modes with flexible tunability is highly desirable.

Coupling direction is another widely discussed topic in SLRs studies. Controlling the coupling direction of SLRs can facilitate many applications, such as optical communication[42]. Under the discrete-dipole model, the oscillation direction or dipole moment of individual resonators determines the coupling direction of SLRs[43]. Most reported plasmonic SLRs are orthogonally coupled, because metallic nanoparticles have a radiative behavior similar to that of electric dipoles (EDs)[44]. Parallel coupling is usually observed in dielectric metasurfaces due to magnetic dipole (MD) modes in large dielectric nanoparticles[45,46]. Although a few parallelly coupled plasmonic SLR phenomena have been observed[32-34,47-49], a rational design protocol to control the coupling direction is still elusive.

Motivated by these demands, we propose and experimentally demonstrate a tunable multimodal guided-SLR (gSLR) that adapts highly asymmetric index environments, through embedding the metasurface in a slab waveguide. The slab waveguide is introduced to modulate the radiation patterns of individual nanoparticles in the array and works in two ways. On one hand, the slab waveguide opens up an in-plane propagating channel for light scattered off nanoparticles in highly contrasted environments, providing access to SLRs. On the other hand, the rich perpendicularly transmitting transverse electric (TE) and transverse magnetic (TM) modes endow gSLRs with multiple resonant modes in both orthogonal and parallel

coupling directions. The resonance peak number and wavelength of each peak in a fixed lattice configuration can be conveniently adjusted by controlling the slab thickness or the index of the cladding. Moreover, the coupling strength of a specific gSLR mode can be tuned by the vertical position of the array in the slab. Strong multimodal gSLRs over visible to near-infrared (VIS-NIR) range is implemented when constructing the metasurface with a gold nano-disk array-on-mirror (AuNDAoM) configuration. The present work will enrich the understanding of physics in SLRs and pave the way to developing novel nano-plasmonic devices.

2 Results and Discussion

2.1 Origin of multimodal gSLRs

The gold nanoparticle array (AuNPA) metasurface under consideration is fabricated on a quartz substrate (n = ~1.45) by a template-based method and annealed to improve its uniformity[50], with lattice constants of 600 nm in the x-direction (p_x) and 550 nm in the y-direction (p_y) (**Fig. 1a**). A rectangular lattice is intentionally chosen here to avoid mode degeneracy so that different gSLR modes can be distinguished by their peak positions in the spectrum. A dielectric thin film with an index higher than that of the substrate and of the superstrate is deposited to form a slab waveguide, with the AuNPA metasurface embedded in the slab (see the inset in **Fig. 1a**). Buried in a slab waveguide, nanoparticles in the metasurface scatter a portion of the incident light into the waveguide. Similar to guided mode resonances (GMRs) [51,52], once the scattered light couples to a guided mode whose wave number is an integer multiple of the metasurface's lattice constants, nanoparticles in the corresponding directions will be re-excited by the guided waves and oscillate in phase, thus triggering a collective resonance. Unlike GMRs where light is coupled into the waveguide through diffractions by gratings and does not interact with the gratings any more, guided waves in the discussed resonances are injected through light scattering by the constituent nanoparticles and re-excite other nanoparticles in the coupling direction, similar to the situation in classical SLRs. Considering the guided-light-induced origin of this kind of resonance, we term it as a guided surface lattice resonance (gSLR). The dispersion relation of a gSLR mode can be derived from the slab waveguide theory as[53,54]

$$\tan\left(\beta_2 t_{\text{slab}}\right) = \frac{\beta_2(c_{21}\beta_1 + c_{23}\beta_3)}{\beta_2^2 - c_{21}\beta_1 c_{23}\beta_3}, \tag{1}$$

where t_{slab} is the thickness of the slab, $\beta_1 = \sqrt{k^2 - n_1^2 k_0^2}$, $\beta_2 = \sqrt{n_2^2 k_0^2 - k^2}$, $\beta_3 = \sqrt{k^2 - n_3^2 k_0^2}$, $k = \sqrt{(2\pi m/p_x)^2 + (2\pi n/p_y)^2}$ are the wave vectors in the coupling direction, $k_0 = 2\pi/\lambda$ is the wave number in a vacuum and λ is the wavelength, c_{21} and c_{23} are coefficients. For TE modes, $c_{21} = c_{23} = 1$, and for TM modes, $c_{21} = n_{\text{slab}}^2/n_{\text{sup}}^2$ and $c_{23} = n_{\text{slab}}^2/n_{\text{sub}}^2$. The cutoff thickness, the minimum thickness of the slab to support guided modes at given wavelengths, can be derived as[53,54]

$$t_c = \frac{\lambda}{2\pi\sqrt{n_{\text{slab}}^2 - n_{\text{sub}}^2}}\left[\arctan\left(c_{21}\sqrt{\frac{n_{\text{sub}}^2 - n_{\text{sup}}^2}{n_{\text{slab}}^2 - n_{\text{sub}}^2}}\right) + j\pi\right], j = 0,1,2,... \tag{2}$$

In an air-photoresist-quartz configuration ($n_{\text{sup}} = 1$, $n_{\text{slab}} = 1.56$, $n_{\text{sub}} = 1.45$), multiple resonance peaks appear once the slab thickness surpasses the cutoff thickness and redshift as t_{slab} increases (**Fig. 1b** and **Fig. S1**). The simulated positions of gSLR modes closely follow the analytical dispersion relationship. To experimentally observe the evolution of gSLR modes, a slab with gradually increasing thickness is prepared by a process of layer-by-layer spin-coating and curing of photoresist (SU-8; see Method for more experimental details). The measured results closely match the simulations (**Fig. 1c, d** and **f**). The peak splits in experimental results are originated from a small portion of obliquely incident light (**Fig. 1c** and **f**)[55]. In the absence of the slab layer, the collective resonances in such a highly index-contrasted environment ($n_{\text{sup}}/n_{\text{sub}} = 1/1.45$) are inhibited (**Fig. 1d**), because of the destructive influences of the substrate[25]. When looking into the radiation pattern of an AuNP on a substrate, it can be found that the pattern is tailored into three lobes, with one into the superstrate and two into the substrate, leaving no section on the horizontal plane (**Fig. 1e**). When the slab thickness is larger than the cutoff thicknesses of low-order guided modes, narrow TE and TM gSLR peaks appear (**Fig. 1f**). By fitting these two peaks with the Fano formula[56], the Q-factors are calculated to be 183 and 440, respectively (**Fig. S5**), which are comparable to reported values for high-Q SLRs[26,36,57,58]. In an environment where the index contrast between the superstrate and substrate is smaller, gSLR modes appear in thinner slabs and redshift compared to those in environments with larger index contrasts (**Fig. S3**). The TM0($\pm$1, 0) gSLR mode has a strength that is much weaker than TE0(0, $\pm$1) (**Fig. 1f**), since

the energy coupled to TM0 mode is smaller than that coupled to TE0 (**Fig. 1g**). It should be noted that TEj(0, ±1) and TMj(±1, 0), j denoting the mode order (j = 0, 1, 2, ...), have perpendicular coupling directions because light coupled to TE and TM modes of the same polarization transfers orthogonally inside the slab (**Fig. 1g**). The coupling direction of TEj(0, ±1) modes is orthogonal to the excitation polarization while that of TMj(±1, 0) modes is parallel (**Fig. 1h** and **i**). The rectangular unit cell makes it easy to differentiate the coupling direction by peak positions. Under x-polarized excitation, TMj(±1, 0) modes are at longer wavelengths (Fig. 2b), because their coupling directions are along the longer axis of the lattice. Slight redshifts of simulated and experimental mode positions relative to the analytical ones are observed at strong peaks (TE0(0, ±1) and TE1(0, ±1) in **Fig. 1b** and **f**), which is caused by their strong coupling strengths[18,23,45]. The strong coupling strength of TE0(0, ±1) mode also causes field confinement and distortion near AuNPs (**Fig. 1h**), which is another evidence for the interactions between the guided light and AuNPs. For weakly coupled TM0(±1, 0) mode, the field distribution is much less distorted (**Fig. 1i**), similar to that of GMRs .

Strong SLRs also occur near the TEj(0, ±1) modes even when the corresponding TE modes are cut-off. This could be attributed to reflections at the finite boundaries[40]. The similar field distribution to TEj(0, ±1) modes implies that these SLRs can transition to gSLRs (**Fig. S6**). A clear evolution path from a SLR to a gSLR can be found in both simulations and experiments that resonances above the TEj modes' cut-off lines transition to TEj(0, ±1) gSLR modes smoothly (**Fig. 1b** and **c**, **Fig. S2**), on account of the transition from ordinary reflection to total internal reflection, with the increase of the slab thickness. However, when guided modes are cut off, TMj and TEj(±1, ±1) modes are totally turned off. This is because ordinary reflections do not modify the radiation pattern as strongly as guided waves do. As shown in **Fig. S6 c** and **e**, little light is scattered in the parallel direction (e.g., x-direction under x-polarized excitation).
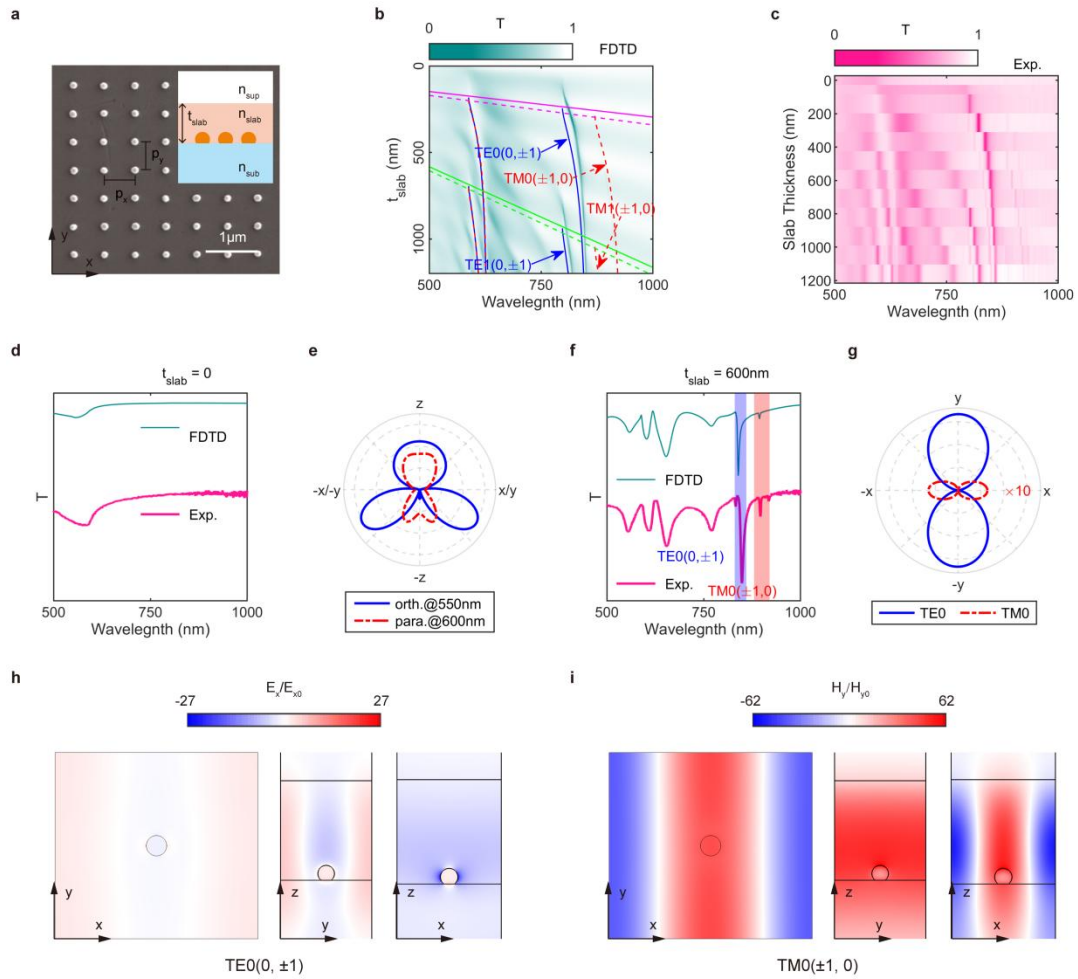
Fig. 1 Multimodal gSLRs. (a) SEM image of a fabricated AuNPA metasurface. Each AuNP has a diameter of ~100 nm and a height of ~90 nm. Lattice constants in the x (p_x) and y (p_y) directions are 600 nm and 550 nm, respectively. Inset: Side-view of the gSLR configuration. The AuNPA is fabricated on a quartz substrate and embedded in a finite polymer slab (SU-8 photoresist). (b) Simulated gSLR modes evolution with the increase of the slab thickness. TEj(0, ±1) and TMj(±1,0) gSLR modes are marked by blue solid and red dashed curves. Unlabeled curves on the left correspond to TEj(±1, ±1) and TMj(±1, ±1) gSLR modes. Solid and dashed straight lines indicate the cutoff thicknesses of TE and TM waveguide modes, specifically, with magenta for TE0 (TM0) and green for TE1 (TM1). (c) Experimental results of gSLR modes evolution. (d) Simulated and measured transmittance spectra of the AuNPA on a quartz substrate with an air cladding. (e) Radiation pattern of a single AuNP on quartz and in air. (f) Simulated and measured gSLR transmittance spectra of the metasurface embedded in a 600-nm-thick slab. Light blue and light red shadows denote the positions of TE0(0, ±1) and TM0(±1,0) gSLR modes, respectively. (g) Guided-mode radiation patterns of a singe AuNP in a 600 nm slab at TE0(0, ±1) and TM0(±1,0) gSLR modes in (f). (h,i) Field distributions of TE0(0, ±1) (h) and TM0(±1,0) (i) gSLR modes.

2.2 Tunable mode strength of gSLRs

Dipole emission inside a waveguide has been proven to be position-dependent[59]. Because the scattering by simple plasmonic nanoparticles can be modeled as EDs[20,44], a reasonable

hypothesis is that gSLRs in a metasurface are positionally tunable. As illustrated in **Fig. 2a**, by changing the vertical position of the metasurface, the radiation patterns of individual nanoparticles can be modulated. Consequently, the corresponding gSLR modes coupling strengths can be controlled. Numerical simulations show that the TE1(0, ±1) mode undergoes an on-off-on transition when the metasurface is elevated from the bottom to the top of a 1200 nm slab, whereas the TM1(±1, 0) mode goes off-on-off. Other gSLR modes also show strength variations during this levitation (**Fig. 2b**). Specifically, when the metasurface is vertically displaced by 500 nm from the bottom of the slab, the TE0(0, ±1) mode redshifts and shows a deeper valley, the originally weak TM0(±1,0) mode is further suppressed, and the strong TE1(0, ±1) mode is totally suppressed while the TM1(±1,0) mode reaches its strongest strength. All these predicted features are confirmed by the experimental results in **Fig. 2c**. To explore the mechanism of the tunability, guided modes radiation patterns of a single AuNP in a waveguide at 0 and 500 nm distances from the substrate surface are calculated. Upon displacing the AuNP upwards, the far field intensity of the TE0 mode gets stronger (**Fig. 2d**), resulting in a stronger gSLR coupling strength as well as a redshifted and strengthened dip in the spectrum. In comparison, the TM0 mode is one order of magnitude weaker in the far-field intensity, accounting for the suppression of the TM0(±1, 0) gSLR mode (**Fig. 2e**). Likewise, the reason for the fading of TE1(0, ±1) gSLR mode lies in the weakening of the far-field electric field, which couples to the TE1 mode at ~820 nm when AuNPs are at the bottom of the slab but becomes two orders of magnitude weaker when the AuNPs are lifted by 500 nm (**Fig. 2f**). Similar arguments apply to the TM1 mode (Fig. 2g). In general, through engineering the radiation patterns of nanoparticles in a metasurface by positioning them at different height in the slab waveguide, gSLR modes can be tuned on-demand.

When the metasurface touches the slab's upper boundary, all gSLR modes wear off. This fading can be attributed to a transition from gSLRs to GMRs[51,52]. When the metasurface is completely outside the slab, gSLRs are prohibited and GMRs emerge, as illustrated in **Fig. 3a**. Compared to gSLRs, GMR modes have higher Q-factors (left panel in **Fig. 3b**). This is because light is coupled into the waveguide via diffractions by the meta-grating, thereby affected less by the lossy AuNPs. In the case of gSLRs, by contrast, coupled light is scattered by the AuNPs and strongly interacts with them as light propagates inside the waveguide,

resulting in stronger damping and lower Q-factors. This explanation is supported by the difference between the field distributions of GMR and gSLR modes. As show in **Fig. 3c**, the enhanced electric field is mainly restrained in the waveguide slab with minor distortions near the AuNPs for the GMR TE0 mode. For the gSLR TE0(0, ±1) mode, although the guided wave characteristics are still obvious, the electric field is more confined near the particles (**Fig. 3d**). The localized field enhancement roots in the strong interactions with AuNPs. Moreover, given that high-order diffractions only carry a small portion of the total incident power, the coupling efficiency of GMRs at normal incidence is usually very low. As a result, the excitation and observation of GMRs need elaborate apparatuses, for example, cross-polarized measurements to exclude uncoupled background noises[51], and because of this, most reported ultra-high-Q GMRs are operated in the reflection mode[51,52]. Nevertheless, the very higher coupling efficiency enabled by scattering makes gSLRs much easier to access. As compared in **Fig. 3b**, under the same experiment conditions, gSLR modes are prominent while GMR modes are hard to recognize. This difference suggests the favorable role of gSLRs in applications that require high coupling efficiencies and high Q-factors, for example, solar energy harvesting[60].
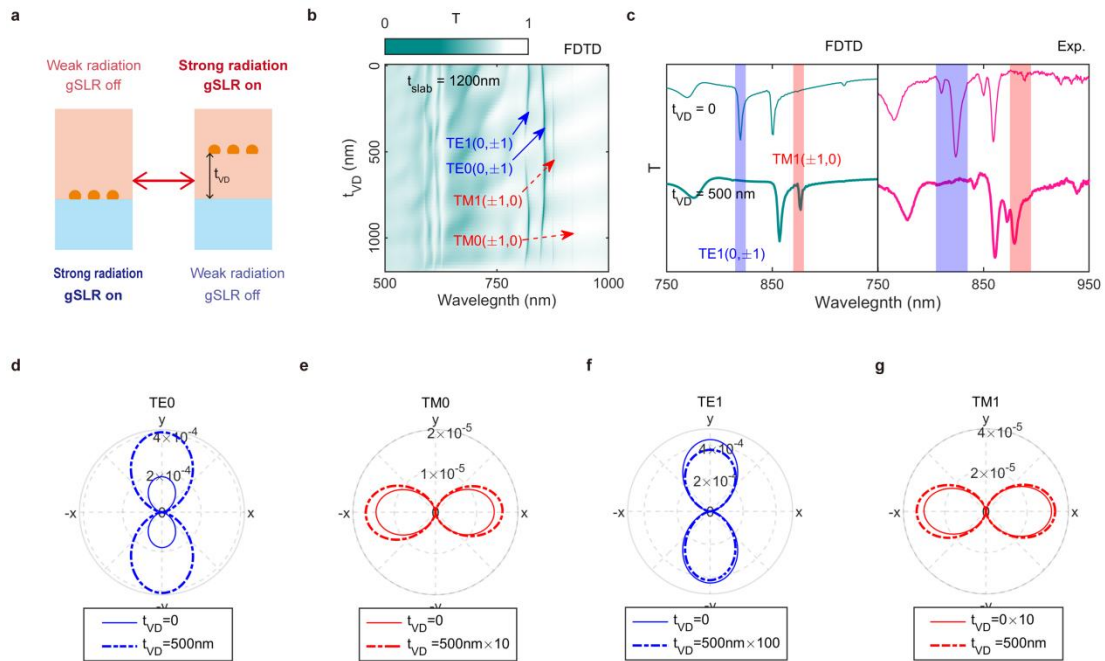

Fig. 2 Tunable mode strength of gSLRs. (a) Schematic of positionally tuning of gSLRs. (b) Simulated tunable gSLRs. (c) Simulated (left) and experimental (right) transmittance spectra of the metasurface with t_{sab} = 1200 nm, t_{VD} = 0 (top) and t_{VD} = 500 nm (bottom). (d-g) Guided

TE0 (d), TM0 (e), TE1 (f) and TM1 (g) modes radiation patterns at $t_{VD} = 0$ (solid lines) and $t_{VD} = 500$ nm (dashed lines).
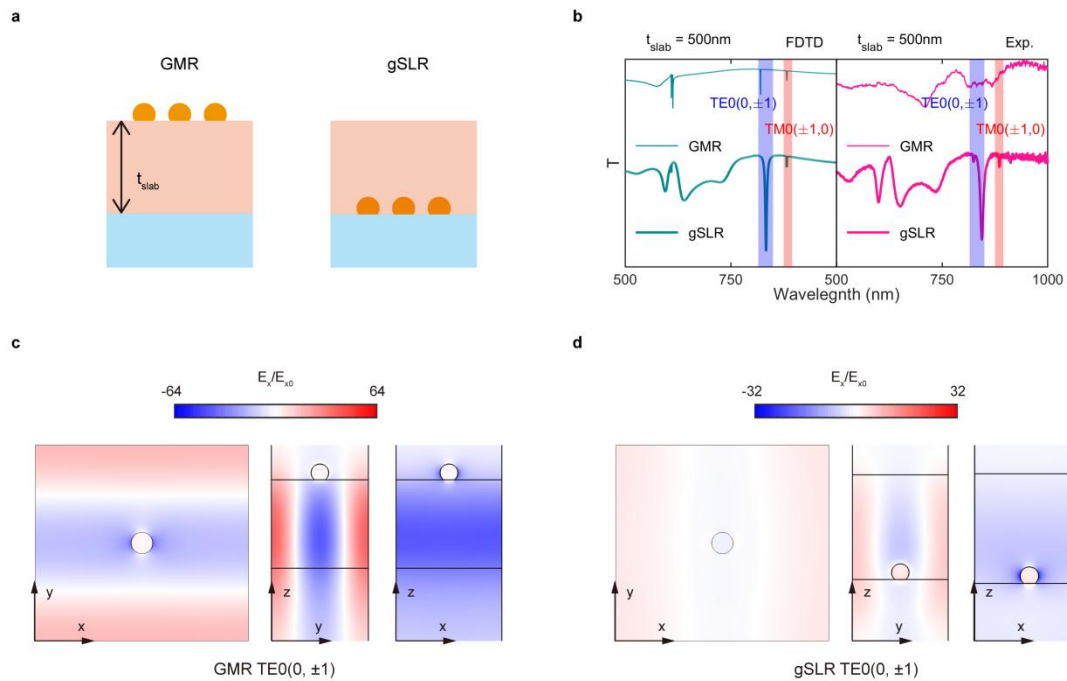

Fig. 3 Comparison between GMRs and gSLRs. (a) Schematics of GMR and gSLR configurations. (b) Simulated and experimental transmittance of GMRs and gSLRs. Vertical strips denote the locations of TE1(0, ±1) and TM1(±1, 0). (c) Electric field distributions of the GMR TE0(0, ±1) mode. (d) Electric field distributions of the gSLR TE0(0, ±1) mode.

2.3 VIS-NIR tunable multimodal gSLRs

Although the gSLRs discussed above have demonstrated good performance in multiple resonances and tunability, two shortcomings still exist with such a dielectric-slab-waveguide configuration: (1) the tunable range of resonance wavelengths is limited, and (2) strong TE and TM gSLR modes are hard to achieve simultaneously. The tuning range is mainly restricted by the index contrast between the slab and the substrate. In the above dielectric slab waveguide, only a 1.56/1.45 slab-to-substrate contrast is implemented. A wider tuning range is achievable by using a metal substrate, which usually have indices lower than unity at optical frequencies. The main difficulty in spectrally overlapping TE and TM modes of gSLRs is how to obtain large electric and magnetic momenta over a wide wavelength range in the same nanostructured resonator. Gold nanoparticle-on-mirror (AuNPoM) cavities are believed to possess these qualities[61-63]. To achieve gSLRs with broad tunable ranges and strong TE and TM modes, a AuNDAoM metasurface is design and prepared, as shown in **Fig. 4a**. **Figure 4b** depicts the magnetic field distribution (color map) and the electric

displacement current (black arrows) of a single AuNPoM cavity under the excitation of an *x*-polarized plane-wave at normal incidence. The electric displacement current forms a loop around the magnetic field hotspot, implying a strong magnetic dipole moment[63]. The extracted radiation pattern of the guided TM0 mode is presented in **Fig. 4c**, showing strong values in the parallel direction (*x*-direction) and zero intensity in the orthogonal direction (*y*-direction). Consequently, a strong lattice resonance with a parallel coupling direction is observed when the metasurface is excited by an *x*-polarized plane wave (**Fig. 4d**), which can be identified as a gSLR TM0(±1, 0) mode after investigating the field distribution (**Fig. 4i**). Similar lattice resonances have been reported by other studies of SLRs in asymmetric environments[32-34], while a clear understanding has been missing. When increasing the slab thickness, the evolution of gSLR modes follows a similar trend as for the above case with a dielectric slab waveguide (**Fig. 4e and f**). Changing the excitation polarization shifts the gSLR modes due to the rectangular lattice configuration (**Fig. S7**). With the presence of the gold substrate, resonance wavelengths can be tuned across the VIS-NIR range, and all the TE and TM gSLR modes are clearly manifest due to the strong electric and magnetic dipole momenta of the AuNPoM cavity. Taking the case where the slab thickness is ~360 nm as an example, as the radiation patterns of TE0 and TM0 modes have comparable intensities (**Fig. 4g**), both TE0(0, ±1) and TM0(±1, 0) gSLR modes create distinct features in the reflectance spectrum (**Fig. 4h**). Strong field confinement near the AuNDs also indicates intensive interactions between light and AuNDs (**Fig. 4j and k**).
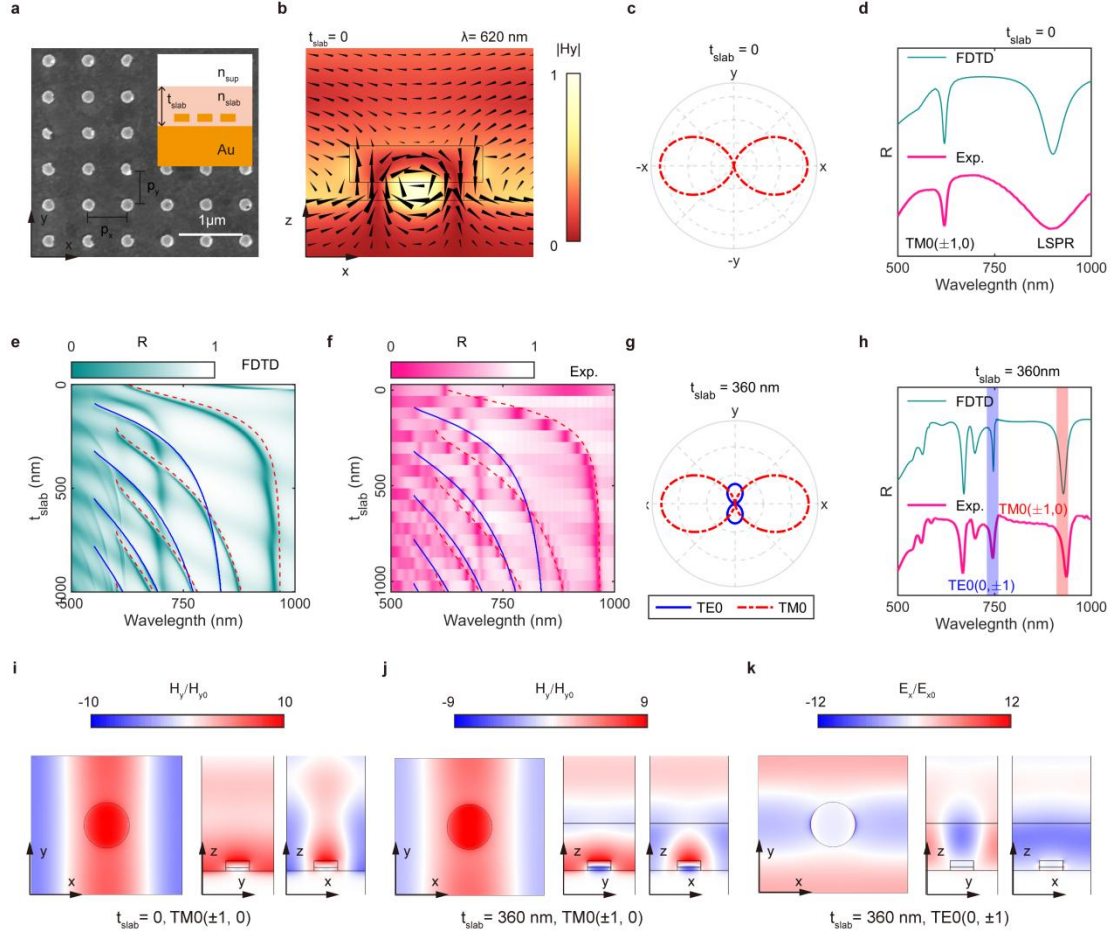
Fig. 4 VIS-NIR tunable multimodal gSLRs in an AuNDAoM metasurface. (a) SEM image of the fabricated AuNDAoM metasurface. Each AuND has a diameter of ~180 nm and a height of ~50 nm. Lattice constants in x (p_x) and y (p_y) directions are 600 nm and 550 nm. Inset shows the side-view of the gSLR configuration. (b) Color map of the normalized magnetic field (H_y) distribution near a resonator, with the black arrows representing the electric displacement current. (c) Radiation pattern of the guided TM0 mode without a slab. (d) Simulated and experimental reflectance spectra of the AuNDAoM metasurface when the slab thickness is 0. (e,f) Simulated (e) and experimental (f) reflectance as functions of slab thickness. Red dashed curves indicate TMj($\pm$1, 0) gSLR modes, and blue solid curves indicate TEj(0,$\pm$1) gSLR modes. From top to bottom, the mode order j is 0, 1, 2, ... (g) Radiation patterns of the guided TM0 and TE0 modes in a 360 nm slab. (h) Simulated and experimental reflectance spectra of the AuNDAoM metasurface when the slab thickness is 360 nm. (i-k) Field distribution of TM0($\pm$1, 0) (i.j) and TE0(0,$\pm$1) (k) gSLR modes.

2.4 Discussions

Firstly, it should be emphasized that the slab waveguide merely modulates the radiation patterns of the nanoparticles inside the slab, rather than altering their optical response. Specifically, no MD can be excited for an AuNP in a slab waveguide, even though TM gSLR modes are arisen from an AuNP lattice. This argument can be supported by calculating the

guided-wave radiation pattern of an ED in a slab waveguide. **Figure S8** shows the tailored radiation pattern of an ED at positions identical to those in the AuNP case in section 2.2. The calculated guided-wave radiation patterns of the ED closely resemble those of an AuNP under the same configuration (**Fig. 1g**), implying that the changes in radiation patterns of AuNPs are induced by the waveguide.

Secondly, although discussions in this manuscript mainly focus on plasmonic dipole lattices, the conclusions and methodology can be applied to multipole and dielectric resonator lattices such as silicon nanoparticles. **Figure S9a** shows simulated results of gSLRs generated in a silicon nanosphere metasurface. Positional tunability is also effective for the all-dielectric metasurface (**Fig. S9b**). The difference is that the TM gSLR modes of dielectric metasurfaces are stronger compared to those of plasmonic metasurfaces in the same configuration, resulting from the intrinsic MDs of large dielectric nanoparticles.

Finally, as discussed earlier, a gSLR supports multiple resonances in orthogonal coupling directions. Taking advantage of the rectangular lattice configuration, the number of modes in one spectrum can be further enriched by altering the excitation polarization. As shown in **Fig. S10**, when the excitation polarization rotates from x- to y-direction, TE0(0, ±1) and TE1(±1, 0) modes transition from their strongest to near zero while the peak intensities of TE1(±1, 0) and TE0(±1, 0) increase from near zero to the highest. Attention should be paid to that unlike being tuned by the vertical position, the resonances' peak positions never change despite the intensity variations. This is because altering the excitation polarization only changes the energy allocations among different gSLR modes. The modal coupling strength or the density-of-state of each mode is determined by the structural configuration and independent of the excitation strength in the linear region.

3 Conclusion

In summary, we have proposed and experimentally demonstrated multimodal gSLRs by embedding the metasurface in a thin dielectric slab. By leveraging the advantages of a slab waveguide to guide light in the metasurface plane, gSLRs can be excited in an asymmetric dielectric environment composed of sharply index-contrasted superstrate and substrate, thereby significantly alleviating the index-matching requirement for conventional SLRs generation. Meanwhile, multimodal resonances with desired mode number, wavelengths and

coupling direction can be readily obtained by adjusting the array lattice constants, slab thickness or cladding index. Moreover, by modifying the radiation patterns of the constituent nanoparticles through vertical positioning the metasurface in the slab, gSLRs are equipped with flexible tunability in mode strength. Strong and tunable gSLR resonances in the VIS-NIR range are also demonstrated with AuNDAoM metasurfaces. The asymmetric-environment-adaptive, easy-to-excite, multimodal and flexibly tunable characteristics of gSLRs will facilitate their potential applications in various fields, such as optoelectronics and biosensors.

Method

Simulations

Finite-difference time-domain (FDTD) simulations were conducted to calculate the scattering cross sections of individual nanoparticles and the transmittance spectra of metasurfaces. For metasurfaces, simulations were performed with a unit cell, using periodic boundary conditions in the in-plane dimensions and perfectly matched layers in the out-of-plane dimension. To improve the convergence, a small negative imaginary part ($k = \sim10^{-4}$) was added to the refractive index of the environment. The free-space and guided radiation patterns of individual nanoparticles were obtained using a finite element method solver (COMSOL) and an open-source algorithm[64].

Sample fabrication

The gold nano-disk array (AuNDA) samples were fabricated using a template-based method. Briefly, a silicon nanohole array mold was created by using electron beam lithography (EBL) and reactive ion etching (RIE). Next, a poly(diallyldimethylammonium chloride) (PDAC) film was deposited onto the mold via spin-coating with a 0.5% aqueous PDAC solution. The nanohole array template was fabricated by depositing 2 nm copper (Cu) and 100 nm silver (Ag) in sequence on the PDAC-capped silicon mold. Upon immersing the mold with the metal film into water, the metal film rapidly floated on the water surface as the highly soluble PDAC dissolved fast in water. To prepare AuNPAs on quartz substrates, the nanohole array template was first transferred onto a quartz substrate. Afterwards, the AuNDA was created by

depositing 1 nm/50 nm Cr/Au and etching the silver template. Finally, the fabricated sample was annealed at 1000 ° C for 2 hours to improve uniformity[50]. For the GMRs sample, the AuNPA lattice was created on a silicon substrate with 285 nm silica using the same procedures, then transferred on to a 500 nm polymer film (SU8) coated on a quartz substrate by etching the silica layer with hydrogen fluoride (HF). For the AuNDAoM samples, the nanohole array template was transferred onto a gold mirror substrate, which was fabricated by spin-coating a thin polymer spacer (SU8, ~25 nm) on an optically thick gold film (~200 nm). After the creation of the AuNDA, the polymer film outside the AuNDs was removed by RIE, exposing the gold substrate to air, i.e. setting t_{slab} to be zero. The slab waveguide was made by spin-coating diluted negative photoresist (SU8-2000.5, diluted five times in anisole) on the sample. The increase in waveguide thickness was achieved through a layer-by-layer coating and curing process.

Optical measurements

The measurement setup is depicted in Fig. S4. Spectra were obtained by a spectrometer under the illumination of a halogen lamp. A 10X objective with a numerical aperture (NA) of 0.3 was used to collect the transmitted signal. An iris was placed at the back focal plane of the objective to ensure that only the plane wave component normal to the metasurface was collected.

Author contributions

S. H. conceived the idea. S. H. and K. Y. performed the simulations. Experiments including sample preparation and optical measurements were conducted by S.H. Experimental results were analyzed by S. H. and K. Y. All the authors contributed to the preparation of the manuscript.

Competing interests

The authors declare no competing interests.

Data availability

The data that support the findings of this study are available in this article and its Supplementary Information. Any other relevant data are available from the corresponding authors upon request.

References

1 Liao, J.-W. *et al.* Highly Localized Surface Plasmon Nanolasers via Strong Coupling. *Nano Letters* **23**, 4359–4366 (2023).

2 Fernandez-Bravo, A. *et al.* Ultralow-threshold, continuous-wave upconverting lasing from subwavelength plasmons. *Nature Materials* **18,** 1172–1176 (2019).

3 Dhama, R. *et al.* All-optical switching based on plasmon-induced Enhancement of Index of Refraction. *Nature Communications* **13**, 3114 (2022).

4 Wang, H. *et al.* All-optical ultrafast polarization switching with nonlinear plasmonic metasurfaces. *Science Advances* **10**, eadk3882 (2024).

5 Mejía-Salazar, J. R. & Oliveira, O. N. Plasmonic Biosensing. *Chemical Reviews* **118**, 10617-10625 (2018).

6 Ahmadivand, A. & Gerislioglu, B. Photonic and Plasmonic Metasensors. *Laser & Photonics Reviews* **16**, 2100328 (2021).

7 Li, G., Zhang, S. & Zentgraf, T. Nonlinear photonic metasurfaces. *Nature Reviews Materials* **2**, 17010 (2017).

8 Li, C. *et al.* Second Harmonic Generation from a Single Plasmonic Nanorod Strongly Coupled to a WSe2 Monolayer. *Nano Letters* **21**, 1599-1605 (2020).

9 Overvig, A. & Alù, A. Diffractive Nonlocal Metasurfaces. *Laser & Photonics Reviews* **16**, 2100633 (2022).

10 Guan, J. *et al.* Far-field coupling between moiré photonic lattices. *Nature Nanotechnology* **18**, 514-520 (2023).

11 Azzam, S. I., Shalaev, V. M., Boltasseva, A. & Kildishev, A. V. Formation of Bound States in the Continuum in Hybrid Plasmonic-Photonic Systems. *Physical Review Letters* **121**, 253901 (2018).

12 Liang, Y. *et al.* Bound States in the Continuum in Anisotropic Plasmonic Metasurfaces. *Nano Letters* **20**, 6351-6356 (2020).

13 Kang, H. *et al.* Stabilization of Silver and Gold Nanoparticles: Preservation and Improvement of Plasmonic Functionalities. *Chemical Reviews* **119**, 664-699 (2018).

14 Wang, M. *et al.* Tunable Fano Resonance and Plasmon–Exciton Coupling in Single Au Nanotriangles on Monolayer WS2 at Room Temperature. *Advanced Materials* **30**, 1705779 (2018).

15 Fang, J. *et al.* Tunable Couplings of Photons with Bright and Dark Excitons in Monolayer Semiconductors on Plasmonic-Nanosphere-on-Mirror Cavities. *The*

Journal of Physical Chemistry C **127**, 9105-9112 (2023).

16   Ma, J., Wang, X., Feng, J., Huang, C. & Fan, Z. Individual Plasmonic Nanoprobes for Biosensing and Bioimaging: Recent Advances and Perspectives. *Small* **17**, 2004287 (2021).

17   Liu, Y. *et al.* Label-Free Ultrasensitive Detection of Abnormal Chiral Metabolites in Diabetes. *ACS Nano* **15**, 6448-6456 (2021).

18   Utyushev, A. D., Zakomirnyi, V. I. & Rasskazov, I. L. Collective lattice resonances: Plasmonics and beyond. *Reviews in Physics* **6**, 100051 (2021).

19   Wang, B. *et al.* High-Q Plasmonic Resonances: Fundamentals and Applications. *Advanced Optical Materials* **9**, 2001520 (2021).

20   Bin-Alam, M. S. *et al.* Ultra-high-Q resonances in plasmonic metasurfaces. *Nature Communications* **12**, 974 (2021).

21   Kravets, V. G., Kabashin, A. V., Barnes, W. L. & Grigorenko, A. N. Plasmonic Surface Lattice Resonances: A Review of Properties and Applications. *Chemical Reviews* **118**, 5912-5951 (2018).

22   Rajeeva, B. B., Lin, L. & Zheng, Y. Design and applications of lattice plasmon resonances. *Nano Research* **11**, 4423–4440 (2018).

23   Auguié, B. & Barnes, W. L. Collective Resonances in Gold Nanoparticle Arrays. *Physical Review Letters* **101** (2008).

24   Auguié, B., Bendaña, X. M., Barnes, W. L. & García de Abajo, F. J. Diffractive arrays of gold nanoparticles near an interface: Critical role of the substrate. *Physical Review B* **82** (2010).

25   Mahi, N. *et al.* In Depth Investigation of Lattice Plasmon Modes in Substrate-Supported Gratings of Metal Monomers and Dimers. *The Journal of Physical Chemistry C* **121**, 2388-2401 (2017).

26   Kelavuori, J. *et al.* Thermal Control of Plasmonic Surface Lattice Resonances. *Nano Letters* **22**, 3879−3883 (2022).

27   Qi, X., Pérez, L. A., Alonso, M. I. & Mihi, A. High Q-Factor Plasmonic Surface Lattice Resonances in Colloidal Nanoparticle Arrays. *ACS Applied Materials & Interfaces* **16**, 1259–1267 (2024).

28   Andreas Tittl, A. L., Mingkai Liu, Filiz Yesilkoy, Duk-Yong Choi, Dragomir N. Neshev, Yuri S. Kivshar, Hatice Altug. Imaging-based molecular barcoding with pixelated dielectric metasurfaces. *Science* **360**, 1105-1109 (2018).

29   Danilov, A. *et al.* Ultra-narrow surface lattice resonances in plasmonic metamaterial arrays for biosensing applications. *Biosensors and Bioelectronics* **104**, 102-112 (2018).

30   Yang, H. *et al.* Detailed formation mechanism of sharp plasmonic lattice modes on Au hemi-ellipsoid arrays in inhomogeneous environment. *Journal of Physics D: Applied Physics* **56** (2023-08-11).

31   Men, D. *et al.* Surface lattice resonance in an asymmetric air environment of 2D Au near-spherical nanoparticle arrays: impact of nanoparticle size and its sensitivity. *Journal of Materials Chemistry C* **12**, 3254 (2024).

32   Li, L. & Wu, W. Bimodal surface lattice resonance sensing based on asymmetric metasurfaces. *Applied Physics Letters* **124**, 071701 (2024).

33   Li, Y. *et al.* Ultra-narrow band perfect absorbance induced by magnetic lattice resonances in dielectric dimer metamaterials. *Results in Physics* **39**, 105730 (2022).

34   Yu, A., Li, W., Wang, Y. & Li, T. Surface lattice resonances based on parallel coupling in metal-insulator-metal stacks. *Optics Express* **26**, 20695 (2018).

35   Guan, J. *et al.* Plasmonic Nanoparticle Lattice Devices for White-Light Lasing. *Advanced Materials* **35**, 2103262 (2021).

36   Wang, D. *et al.* Band-edge engineering for controlled multi-modal nanolasing in plasmonic superlattices. *Nature Nanotechnology* **12**, 889-894 (2017).

37   Baur, S., Sanders, S. & Manjavacas, A. Hybridization of Lattice Resonances. *ACS Nano* **12**, 1618-1629 (2018).

38   Braïk, M. *et al.* Hybridization of surface lattice modes: towards plasmonic metasurfaces with high flexible tunability. *Nanophotonics* **12**, 2179–2188 (2023).

39   Lim, T.-L. *et al.* Fourier-Engineered Plasmonic Lattice Resonances. *ACS Nano* **16**, 5696–5703 (2022).

40   Reshef, O. *et al.* Multiresonant High-Q Plasmonic Metasurfaces. *Nano Letters* **19**, 6429-6434 (2019).

41   Volk, K., Fitzgerald, J. P. S. & Karg, M. In-Plane Surface Lattice and Higher Order Resonances in Self-Assembled Plasmonic Monolayers: From Substrate-Supported to Free-Standing Thin Films. *ACS Applied Materials & Interfaces* **11**, 16096-16106 (2019).

42   Boddeti, A. K. *et al.* Long-Range Dipole–Dipole Interactions in a Plasmonic Lattice. *Nano Letters* **22**, 22-28 (2021).

43   Huttunen, M. J., Dolgaleva, K., Törmä, P. & Boyd, R. W. Ultra-strong polarization dependence of surface lattice resonances with out-of-plane plasmon oscillations. *Optics Express* **24**, 28279 (2016).

44   Novotny, L. & van Hulst, N. Antennas for light. *Nature Photonics* **5**, 83-90 (2011).

45   Zakomirnyi, V. I. *et al.* Collective lattice resonances in arrays of dielectric nanoparticles: a matter of size. *Optics Letters* **44,** 5743-5746 (2019).

46   Li, J., Verellen, N. & Van Dorpe, P. Engineering electric and magnetic dipole coupling in arrays of dielectric nanoparticles. *Journal of Applied Physics* **123**, 083101 (2018).

47   Lin, L. & Yi, Y. Orthogonal and parallel lattice plasmon resonance in core-shell SiO2/Au nanocylinder arrays. *Optics Express* **23**, 224136 (2015).

48   Vitrey, A., Aigouy, L., Prieto, P., García-Martín, J. M. & González, M. U. Parallel Collective Resonances in Arrays of Gold Nanorods. *Nano Letters* **14**, 2079-2085 (2014).

49   Muravitskaya, A., Movsesyan, A., Kostcheev, S. & Adam, P.-M. Polarization switching between parallel and orthogonal collective resonances in arrays of metal nanoparticles. *Journal of the Optical Society of America B* **36**, 65-70 (2019).

50   Deng, S. *et al.* Ultranarrow plasmon resonances from annealed nanoparticle lattices. *Proc Natl Acad Sci U S A* **117**, 23380-23384 (2020).

51   Huang, L. *et al.* Ultrahigh-Q guided mode resonances in an All-dielectric metasurface. *Nature Communications* **14**, 3433 (2023).

52   Quaranta, G., Basset, G., Martin, O. J. F. & Gallinet, B. Recent Advances in Resonant

Waveguide Gratings. *Laser & Photonics Reviews* **12**, 1800017 (2018).

53   Hunsperger, R. G. Integrated Optics: Theory and Technology. (Springer, 2009).

54   Snyder, A. W. & Love, J. D. Optical Waveguide Theory. (Springer, 1984).

55   Gutha, R. R., Sadeghi, S. M., Sharp, C., Hatef, A. & Lin, Y. Multi-order surface lattice resonances and dark mode activation in metallic nanoantenna arrays. *Journal of Applied Physics* **125**, 023103 (2019).

56   Luk'yanchuk, B. et al. The Fano resonance in plasmonic nanostructures and metamaterials. *Nature Materials* **9**, 707-715 (2010).

57   Le-Van, Q. *et al.* Enhanced Quality Factors of Surface Lattice Resonances in Plasmonic Arrays of Nanoparticles. *Advanced Optical Materials* **7**, 1801451 (2019).

58   Yang, F. *et al.* Fabrication of Centimeter-Scale Plasmonic Nanoparticle Arrays with Ultranarrow Surface Lattice Resonances. *ACS Nano* **17**, 725-734 (2022).

59   Ramezani, M., Lozano, G., Verschuuren, M. A. & Gómez-Rivas, J. Modified emission of extended light emitting layers by selective coupling to collective lattice resonances. *Physical Review B* **94**, 125406 (2016).

60   Zhukovsky, S. V. *et al.* Enhanced Electron Photoemission by Collective Lattice Resonances in Plasmonic Nanoparticle-Array Photodetectors and Solar Cells. *Plasmonics* **9**, 283–289 (2014).

61   Tserkezis, C. et al. Hybridization of plasmonic antenna and cavity modes: Extreme optics of nanoparticle-on-mirror nanogaps. *Physical Review A* **92**, 053811 (2015).

62   Huang, Y., Ma, L., Li, J. & Zhang, Z. Nanoparticle-on-mirror cavity modes for huge and/or tunable plasmonic field enhancement. *Nanotechnology* **28**, 105203 (2017).

63   Liu, Y. et al. Compact Magnetic Antennas for Directional Excitation of Surface Plasmons. *Nano Letters* **12**, 4853-4858 (2012).

64   Yang, J., Hugonin, J.-P. & Lalanne, P. Near-to-Far Field Transformations for Radiative and Guided Waves. *ACS Photonics* **3**, 395-402 (2016).

Supporting Information

Tunable Multimodal Guided Surface Lattice Resonances in Index-Discontinuous Environments

Suichu Huang[1], Kan Yao[2], Wentao Huang[1], Xuezheng Zhao[1, *], Yuebing Zheng[2, *], Yunlu Pan[1, *]

1 Key Laboratory of Micro-Systems and Micro-Structures Manufacturing of Ministry of Education and School of Mechatronics Engineering, Harbin Institute of Technology, Harbin 150001, China

2 Walker Department of Mechanical Engineering, Material Science and Engineering Program and Texas Materials Institute, The University of Texas at Austin, Austin, TX 78712, United States

*Corresponding author. Email: zhaoxz@hit.edu.cn, zheng@austin.utexas.edu, yunlupan@hit.edu.cn

Section 1 Waveguided modes in a three-layer slab waveguide and gSLR

When $n_2 > n_3 \geq n_1$, a three-layer structure forms a slab waveguide. We firstly consider the transverse electric (TE, E//y) case. For the guided modes, the field intensity goes to zero at the infinity. So the electric field can be expressed as

$$E_y(z) = A\exp(-\beta_1 z), z > \frac{t}{2} \tag{1-1.a}$$

$$E_y(z) = B\cos(\beta_2 z + \varphi), -\frac{t}{2} \leq z \leq \frac{t}{2} \tag{1-1.b}$$

$$E_y(z) = C\exp(\beta_3 z), z < -\frac{t}{2}, \tag{1-1.c}$$

where, $\beta_1 = \sqrt{k^2 - n_1^2 k_0^2}$, $\beta_2 = \sqrt{n_2^2 k_0^2 - k^2}$, $\beta_3 = \sqrt{k^2 - n_3^2 k_0^2}$, and $k = \sqrt{k_x^2 + k_y^2}$ is the in-planar wave number component.

Given

$$H_x = -\frac{i}{\omega\mu_0}\frac{\partial E_y}{\partial z}, \tag{1-2}$$

The magnetic field can be derived as

$$H_x(z) = \frac{i}{\omega\mu_0}\beta_1 A\exp(-\beta_1 z), z > \frac{t}{2} \tag{1-3.a}$$

$$H_x(z) = \frac{i}{\omega\mu_0}\beta_2 B\sin(\beta_2 z + \varphi), -\frac{t}{2} \leq z \leq \frac{t}{2} \tag{1-3.b}$$

$$H_x(z) = -\frac{i}{\omega\mu_0}\beta_3 C\exp(\beta_3 z), z < -\frac{t}{2}. \tag{1-3.c}$$

Since E_y and H_x are continuous at the interfaces, we have

$$A\exp\left(-\beta_1\frac{t}{2}\right) = B\cos\left(\beta_2\frac{t}{2} + \varphi\right) \tag{1-4.a}$$

$$D\exp\left(-\beta_3\frac{t}{2}\right) = B\cos\left(-\beta_2\frac{t}{2} + \varphi\right) \tag{1-4.b}$$

$$\beta_1 A\exp\left(-\beta_1\frac{t}{2}\right) = \beta_2 B\sin\left(\beta_2\frac{t}{2} + \varphi\right) \tag{1-4.c}$$

$$-\beta_3 A\exp\left(-\beta_1\frac{t}{2}\right) = \beta_2 B\sin\left(-\beta_2\frac{t}{2}+\varphi\right) \tag{1-4.d}$$

$$\beta_1 \cdot (2-4.a)-(2-4.c): \qquad \tan\left(\beta_2\frac{t}{2}+\varphi\right)=\frac{\beta_1}{\beta_2} \tag{1-5.a}$$

$$\beta_3 \cdot (2-4.b)+(2-4.d): \qquad \tan\left(-\beta_2\frac{t}{2}+\varphi\right)=-\frac{\beta_3}{\beta_2} \tag{1-5.b}$$

By eliminating φ, the dispersion relationship of TE modes is

$$\tan(\beta_2 t) = \frac{\beta_2(\beta_1+\beta_3)}{\beta_2^2-\beta_1\beta_3} . \tag{1-6}$$

Similarly, the dispersion relationship of TM modes is

$$\tan(\beta_2 t) = \frac{\beta_2(c_{21}\beta_1+c_{23}\beta_3)}{\beta_2^2-c_{21}\beta_1 c_{23}\beta_3} , \tag{1-7}$$

where, $c_{21}=\frac{n_2^2}{n_1^2}$, $c_{23}=\frac{n_2^2}{n_3^2}$.

The effective index ($n_{\text{eff}}=k/k_0$) of each mode can be obtain by solving (1-6) and (1-7). For a given configuration, the cut-off wavelength is

$$\lambda_c = \frac{2\pi t\sqrt{n_2^2-n_3^2}}{\left[arctan\left(c_{21}\sqrt{\frac{n_3^2-n_1^2}{n_2^2-n_3^2}}\right)+j\pi\right]}, j = 0,1,2,\ldots \tag{1-8}$$

Where, for TE modes, $c_{21}=1$, for TM modes, $c_{21}=\frac{n_2^2}{n_1^2}$.

And for a given wavelength, the cut-off thickness of the slab is

$$t_c = \frac{\lambda}{2\pi\sqrt{n_2^2-n_3^2}}\left[arctan\left(c_{21}\sqrt{\frac{n_3^2-n_1^2}{n_2^2-n_3^2}}\right)+j\pi\right], j = 0,1,2,.. \tag{1-9}$$

The out-side in-coming light would not couple to these waveguided modes. However, should there be small structures inside the waveguide, some of the scattered light can match wave vectors of guided modes and thus transmits planarly inside the waveguide core layer. If the structure is an array, the travelling scattered light from nearby units will couple to each other, once their in-plane wave vectors satisfy

$$k_x = \frac{2\pi m}{P_x} \tag{1-10.a}$$

$$k_y = \frac{2\pi n}{P_y} \tag{1-10.b}$$

where m = 0,1 2, ..., n = 0,1 2, ... and $m^2+n^2 \neq 0$.

The origin of this kind of in-plane coupling is the same as surface lattice resonance (SLR), in which we define it as guided surface lattice resonance (gSLR). Substituting (1-10) into (1-6, 1-7), possible gLSR peaks positions can be determined. Taking advantages of rich modes of waveguides, gSLR possesses a multimodal nature. Figure S1 plots the mode evolution with slab thickness of a rectangular metasurface with lattice constants of 600 nm and 550 nm in x- and y-direction and under x-polarized normal incidence.
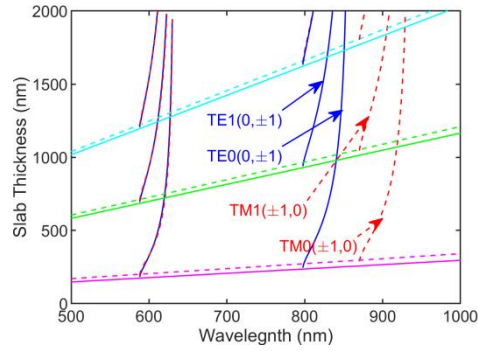
Fig. S1 Guided-SLR modes of a rectangular metasurface. Indices of the three-layer structure are 1, 1.56 and 1.45, respectively. Lattice constants are 600 nm and 550 nm in *x*- and *y*-direction, and the excitation is *x*-polarized. Solid and dash lines indicate cut-off thickness with solid lines for TE modes, dash lines for TM modes. From bottom to top, lines represent TE0, TM0, TE1, TM1, TE2 and TM2.
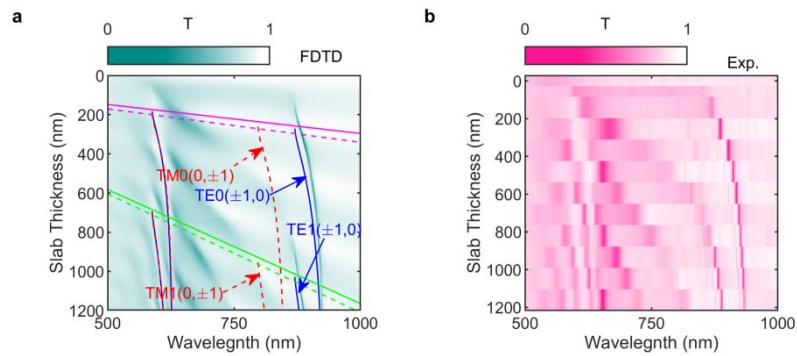

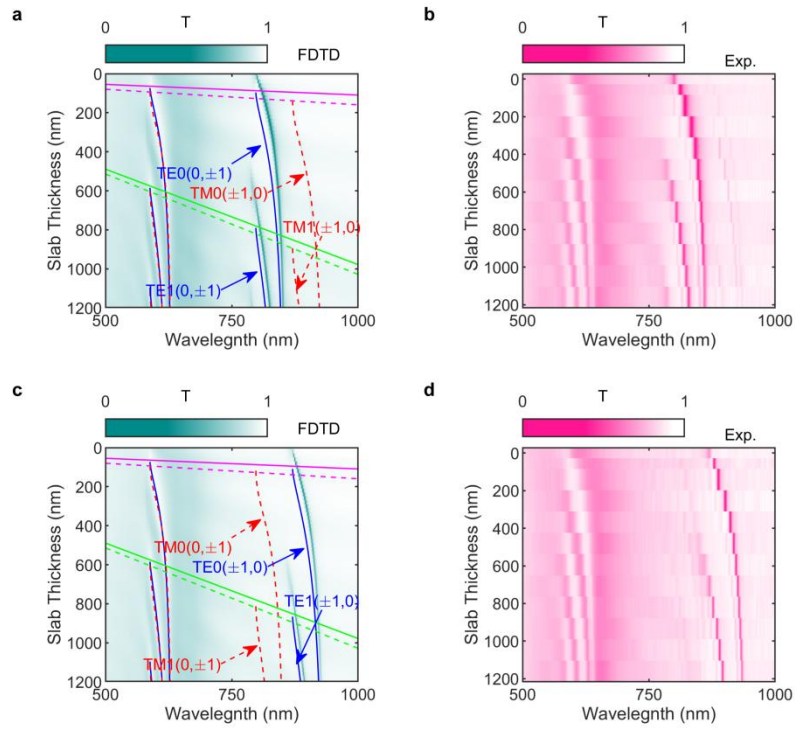**Fig. S2 Mode evolution of gSLR under *y*-polarized excitation in Air superstrate**.

Fig. S3 Guided-SLR in EG superstrate. (a) Simulated transmittance spectra mapping in EG superstrate under *x*-polarized excitation, gLSR modes are labeled, (b) Experiment transmittance spectra mapping in EG superstrate under *x*-polarized excitation, (c) Simulated transmittance spectra mapping in EG superstrate under *y*-polarized excitation, gLSR modes are labeled, (d) Experiment transmittance spectra mapping in EG superstrate under *y*-polarized excitation.
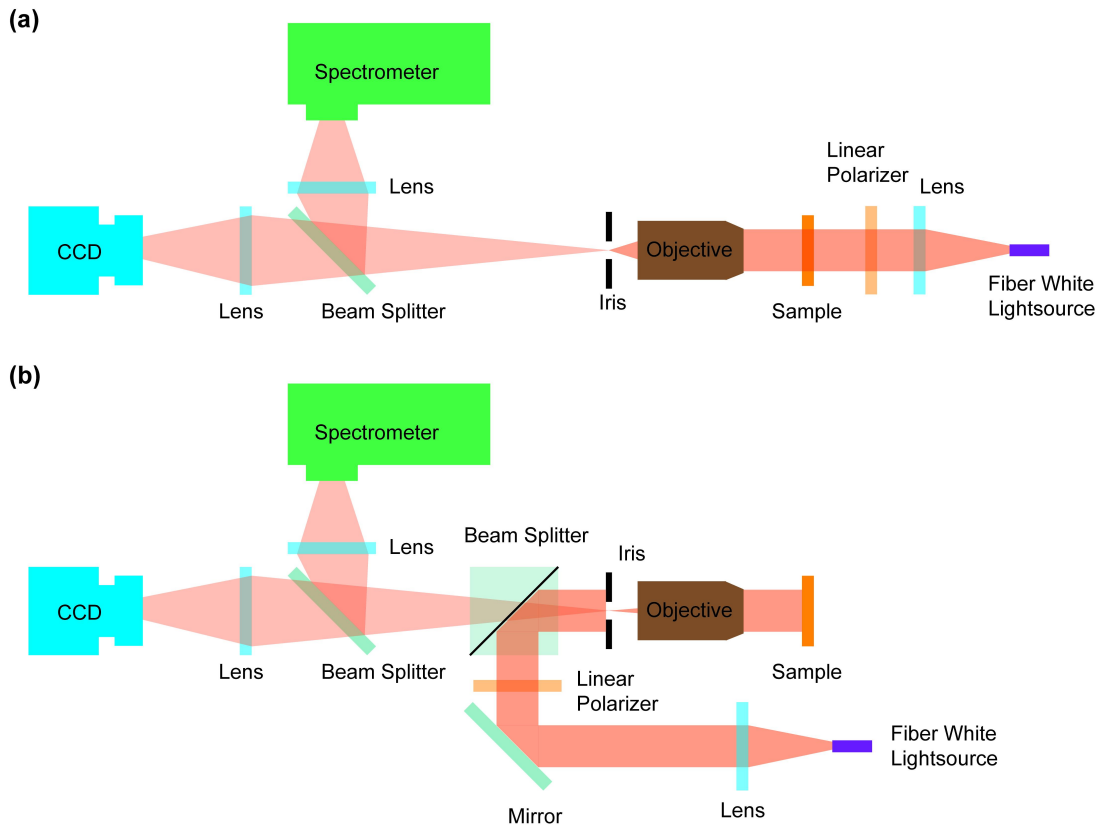
Fig. S4 Experimental set-up. (a) Transmittance spectra measurement set-up. (b) Reflectance spectra measurement set-up
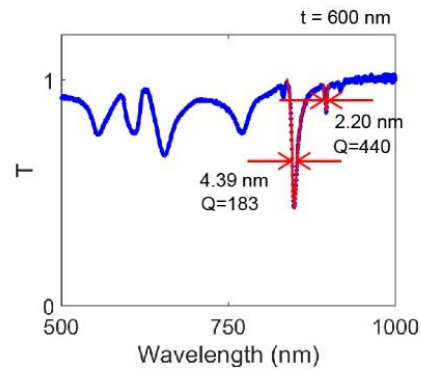
Fig. S5 Fano fitting and Q-factors of g-SLR.
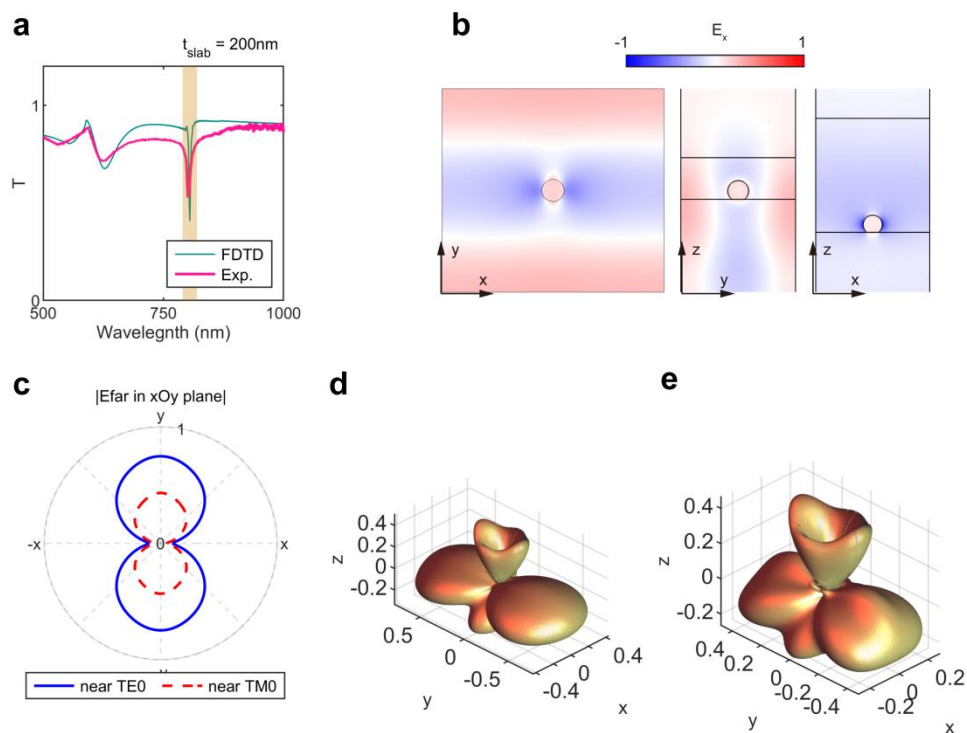
Fig. S6 SLR generated by ordinary reflections of a finite boundary. (a) Simulated and experimental transmittance spectra. (b) Electric field distribution. (c) Far-field radiation pattern in the *xOy* plane. (d) 3D far-field radiation pattern near TE0(0, ±1). (e) 3D far-field radiation pattern near TM0(±1,0).
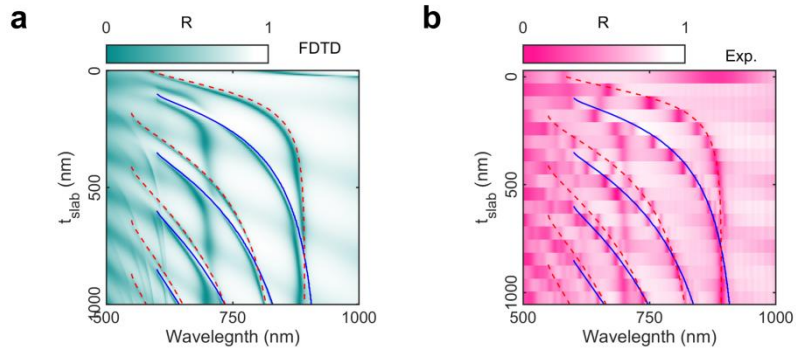
Fig. S7 Mode evolution of gSLRs in the AuNDAoM metasurface under _y_-polarized excitation.
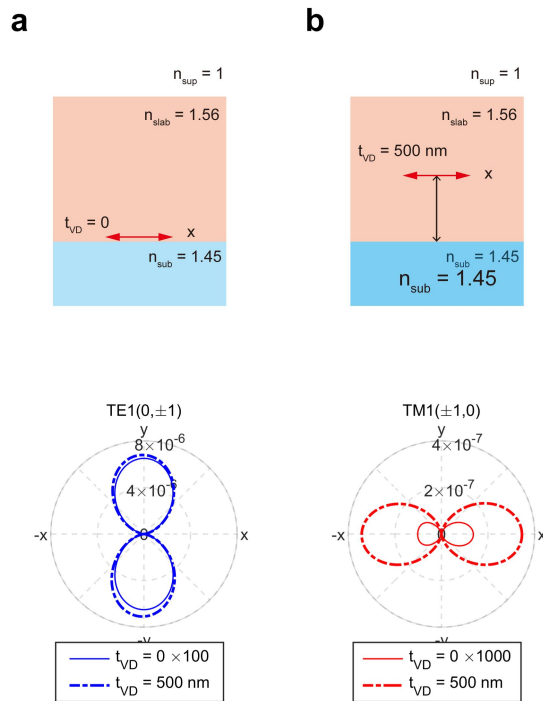

Fig. S8 Slab waveguide modulated radiative pattern of an electric dipole. Radiation pattern of an electric dipole near the boundary of the slab (a) and vertically displaced by 500 nm (b).
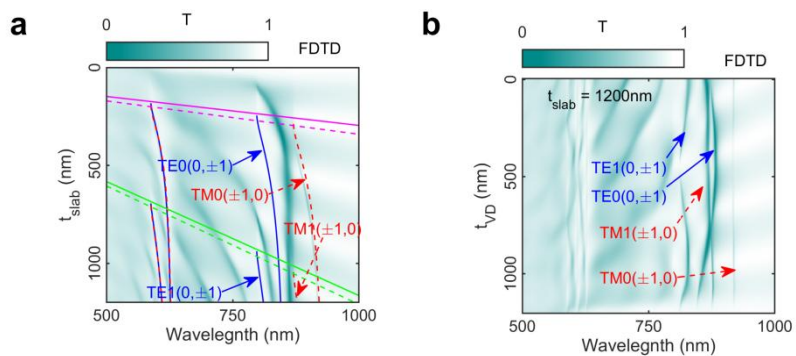
Fig. S9 Guided-SLR mode evolution of a silicon nanoparticle array metasurface. The metasurface consists of silicon nanospheres with a diameter of 130 nm. The lattice configuration is the same as AuNPA metasurface. (a) gSLR mode evolution with the increase of slab thickness. (b) gSLR mode tunability by metasurface vertical position in slab.
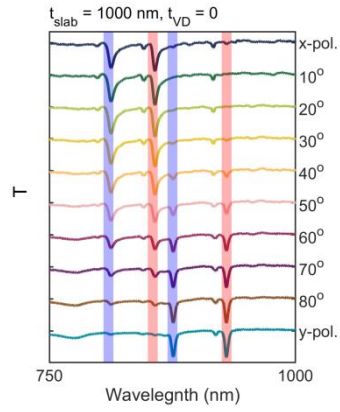

Fig. S10 Excitation polarization switching gSLR. The shadowed strips indicate TE1(0, ±1), TE0(0, ±1), TE1(±1, 0) and TE0(±1, 0) from left to right.